Tong Jia[1,2], Jianjun Liang[1,3], Xiao-Ming Li[1,3], and Qiang Li[4]

[1] Key Laboratory of Digital Earth Science, Aerospace Information Research Institute, Chinese Academy of Sciences, Beijing, China.

[2] University of Chinese Academy of Sciences, Beijing, China.

[3] Key Laboratory of Earth Observation of Hainan Province, Hainan Research Institute, Aerospace Information Research Institute, Chinese Academy of Sciences, Sanya, China.

[4] Graduate School at Shenzhen, Tsinghua University, Shenzhen, China.

Corresponding author: Xiao-Ming Li (lixm@radi.ac.cn)

Key Points:

- Generation of nonlinear internal waves (NLIWs) on the northern continental shelf south of Hainan Island is revealed by a synergistic analysis of satellite observations, in situ measurements and numerical simulations.
- Various sources and mechanisms in Xisha Islands can excite the generation of NLIWs on the shelf.
- Locally generated shoreward internal tides emanating from the shelf break contribute little to the generation of NLIWs on the shelf.

Abstract

Nonlinear internal waves (NLIWs) are prevalent on the northern continental shelf south of Hainan Island in the South China Sea. However, our understanding of these NLIWs is still in a preliminary state. In the study, through a synergistic analysis of satellite observations, in situ measurements and numerical simulations, we take a step toward fully elucidating the generation and propagation process of the NLIWs on the northern continental shelf south of Hainan Island. Both mooring and satellite observations suggest that the Xisha Islands remotely generate the NLIWs on the northern continental shelf south of Hainan Island; moreover, more than one source exists in the Xisha Islands. Based on the realistic topography, stratification and tidal forcing, two-dimensional numerical simulations using the MITgcm reveal that the NLIWs observed on the continental shelf can be generated from different sills in Xisha Islands through the internal tidal beam or mixed tidal lee wave regime. Furthermore, the internal tide energy flux estimation suggests that the locally generated internal tides emanating from the continental shelf break play an essential role in the baroclinic energy field of the deep sea while their influence on the baroclinic energy field of the mid-continental shelf can be almost negligible.

Plain Language Summary

Nonlinear internal waves (NLIWs) are internal gravity waves that are characterized by significant perturbations in the current and density distributions of the ocean. They are widely observed on the northern continental shelf south

of Hainan Island in the South China Sea, yet their generation are rarely reported. Satellite observations, in situ measurements, and numerical simulations are three effective ways to study NLIWs. Our previous study, based on the spaceborne synthetic aperture radar (SAR) observation and theoretical analysis, preliminarily analyzed the generation sources and mechanisms of the NLIWs on the northern continental shelf south of Hainan Island; however, in situ observations and numerical simulations are lack in the study. Therefore, the exploration for the generation of NLIWs on the northern continental shelf south of Hainan Island is insufficient. In this study, the generation of the NLIWs on the northern continental shelf south of Hainan Island is further investigated by a combination of satellite observations, in situ measurements, and numerical simulations. It is found that the NLIWs observed on the northern continental shelf south of Hainan Island can be generated by different sills in the Xisha Islands through the internal tidal beam or mixed tidal lee wave regime. Moreover, the local internal tides generated from the continental shelf break are found to play a crucial role in the deep ocean, while their influence on the mid-continental shelf can be almost negligible.

1 Introduction

Nonlinear internal waves (NLIWs) are ubiquitous in continental and coastal oceans, and are often characterized by strong perturbations and currents in the water column stratification (Alford et al., 2015; Garrett & Munk, 1979; Huang et al., 2016; Jackson et al., 2012). These powerful internal motions in the ocean pose a significant threat to the subsurface navigation and offshore energy development (Duda & Preisig, 1999; Lynch et al., 2010; Osborne et al., 1978; Shanks, 1987). Moreover, NLIWs contribute largely to local turbulent dissipation and diapycnal mixing during their breaking and dissipation (Fer et al., 2020; Lamb, 2014; Moum et al., 2003; Sandstrom & Oakey, 1995), with significant effects on coastal nutrients transport, biological productivity and water-borne constituents such as contaminants and sediments (Heathershaw, 1985; Pomar et al., 2012; Quaresma et al., 2007; Sandstrom & Elliott, 1984; Shanks, 2021; Woodson, 2018).

Satellite observations, in situ measurements, and numerical simulations are three important ways to study the NLIWs in the coastal environment (Liang et al., 2019; Mendes et al., 2021). Though NLIWs propagate within the ocean interior, they are visible from space in both optical remote sensing and synthetic aperture radar (SAR) images due to the modulation of sea surface roughness by the internal wave-induced sea surface currents (Alpers, 1985; Klemas, 2012). Satellite observations provide a vast two-dimensional internal wave field that allows the determination of spatial parameters and frequent occurrence regions, as well as the possible generation and evolution mechanisms of NLIWs (Klemas, 2012; Raju et al., 2019; Tensubam et al., 2021; Zhang & Li, 2020; Zhao et al., 2004; Zhao et al., 2014). One challenge is that satellite observation cannot directly measure the vertical properties of NLIWs, such as the wave amplitude. In situ measurements can access the three-dimensional structure of NLIWs by

recording hydrodynamic parameters in the ocean (e.g., the temperature and velocity), which, however, are sparse and only provide information at point locations. Thus, it is not easy to elaborate on the generation and propagation of NLIWs via the in situ measurement in a given region. Recent progress in developing the numerical simulation provides new insights into the study of NLIWs and enables finer details of internal wave motion at a low cost. Classical numerical models for investigating the internal waves properties include the ROMS (Kanarska et al., 2007), SUNTANS (Fringer et al., 2006) and MITgcm (Marshall et al., 1997). These numerical models can simulate and reproduce the wave generation and propagation process by setting up the appropriate model environment; however, the model parameters are often selected based on the in situ and satellite observations. Overall, combing all three methods is the optimum choice for a comprehensive understanding of internal waves.

The generation of NLIWs over coastal/shelf topography is complex. On these regions, NLIWs often arise from the tidal flow over bottom topography by the release of internal lee waves or hydraulic jumps (Apel et al., 1997; Maxworthy, 1979), the interaction of internal tidal beams with pycnocline (Cole et al., 2009; Gerkema, 2001; Pingree & New, 1991; Vlasenko & Stashchuk, 2015), or the transformation of the internal tide (Buijsman et al., 2010; Helfrich & Grimshaw, 2008; Lee & Beardsley, 1974). In some unique coastal regions, remote source may result in the observed NLIWs behaving unpredictably, thus increasing the complexity of the studied NLIW field (Nash et al., 2012; Small et al., 1999; Zhang et al., 2015). The northern continental shelf south of Hainan Island in the South China Sea (SCS) represents one such example. Based on the SAR observation and theoretical analysis, our preliminary study (Jia et al., 2021) has suggested that the NLIWs observed on the northern continental shelf south of Hainan Island (Figure 1) are generated from the Xisha Islands; however, in situ observation and numerical simulation are lack in the study. Therefore, the exploration for the generation of the NLIWs on the northern continental shelf south of Hainan Island is insufficient.

Moreover, the continental shelf break is an essential source of the internal tide, so a further question arises: whether the locally generated internal tides (LITs) formed at the shelf break can interact with the remotely generated internal tides (RITs) coming from Xisha Islands, and consequently influence the generation of the NLIWs on the shelf? In addition, the topography of the Xisha Islands is complicated, and many sills in Xisha Islands have the potential to generate internal tides. So, is there more than one source in Xisha Islands for generating the NLIWs on the shelf? All these questions deserve further investigation. The study employs satellite observation, field measurement, and a high-resolution numerical model to address these questions.

The study is organized as follows: In Section 2, the in situ data, satellite data, numerical model, and method for estimating the internal tide energy flux are introduced. Section 3 reveals the internal wave characteristics from the in situ and satellite observations, and the remote generation mechanism from the nu-

merical simulation. Discussion of the results is presented in Section 4, followed by conclusions in Section 5.

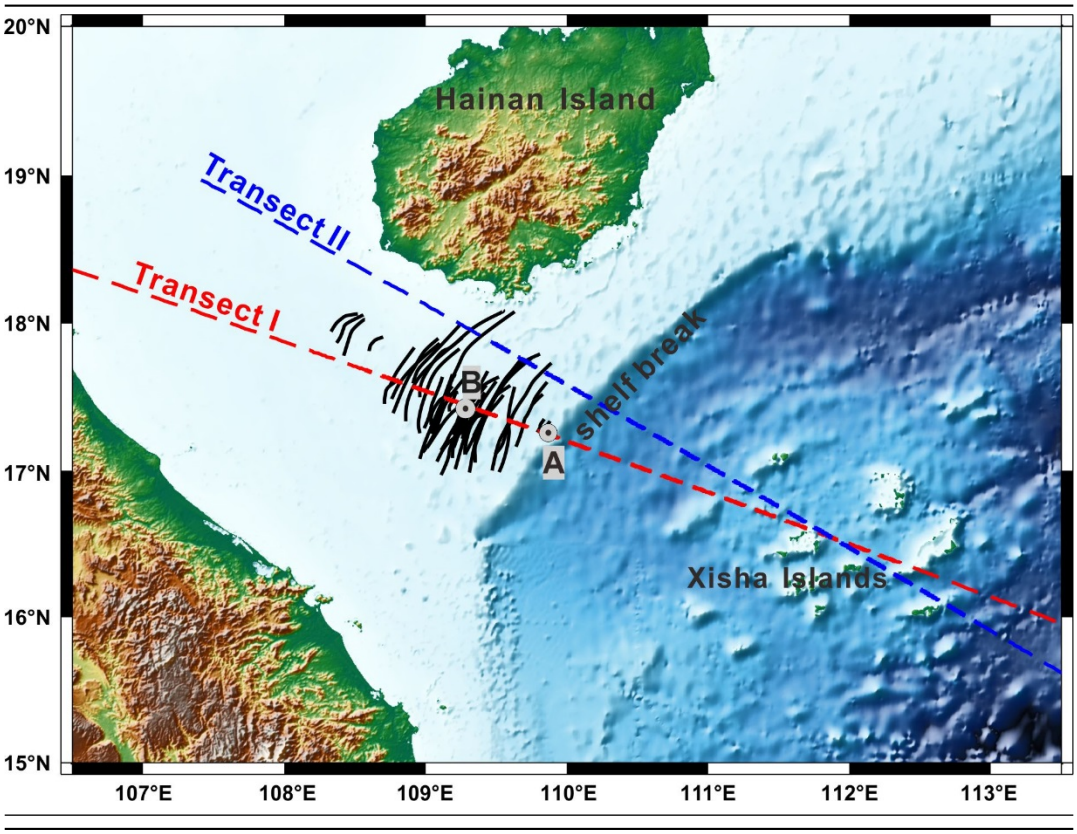

Figure 1. Draft diagram of nonlinear internal waves (NLIWs) on the northern continental shelf south of Hainan Island (adapted from Jia et al., 2021). The black curves indicate the distribution of NLIWs observed in the ENVISAT Advanced SAR and ALOS Phased Array type L-band SAR images from 2002 to 2012 (Jia et al., 2021). The dashed red and blue lines represent two transects I and II taken for the numerical simulation of NLIWs observed on the Gaofen-3 (GF-3) SAR image. The background color indicates the bottom topography. The two grey points denote the locations of moorings A and B.

2 Methodology

2.1 In situ data

From May 31 to June 6, 2021, we made two consecutive mooring observations (A and B in Figure 1) on the northern continental shelf south of Hainan Island to observe internal waves that shoal across a shelf-slope onto the mid-continental shelf.

The mooring locations were chosen based on the distributions of NLIWs observed in the area (Figure 1). Mooring A was deployed at 17°16.33 N/109°52.45 E, in a water depth of 179.5 m over the continental slope, from May 31 to June 3, 2021. From June 4 to June 6, mooring B was performed at 17°25.99 N/109°17.66 E, in a water depth of 106 m over the mid-shelf area. Each mooring (Figure 2) was equipped with a set of thermistor instruments and an upward-looking 300 kHz acoustic Doppler current profiler (ADCP) to obtain the through-water-column temperature and velocity profile time series. The deployed thermistor instruments were set to sample every 1 s to measure the temperature with/without pressure covering almost the entire water column. The deployed ADCPs (at a depth of 93.25 m and 87.5 m, respectively) were set to collect the velocity and direction of the ocean current in the upper part of the water column every 1 min. CTD casts were made hourly during the mooring observations from an anchored vessel near the mooring location to obtain the background stratification profile.

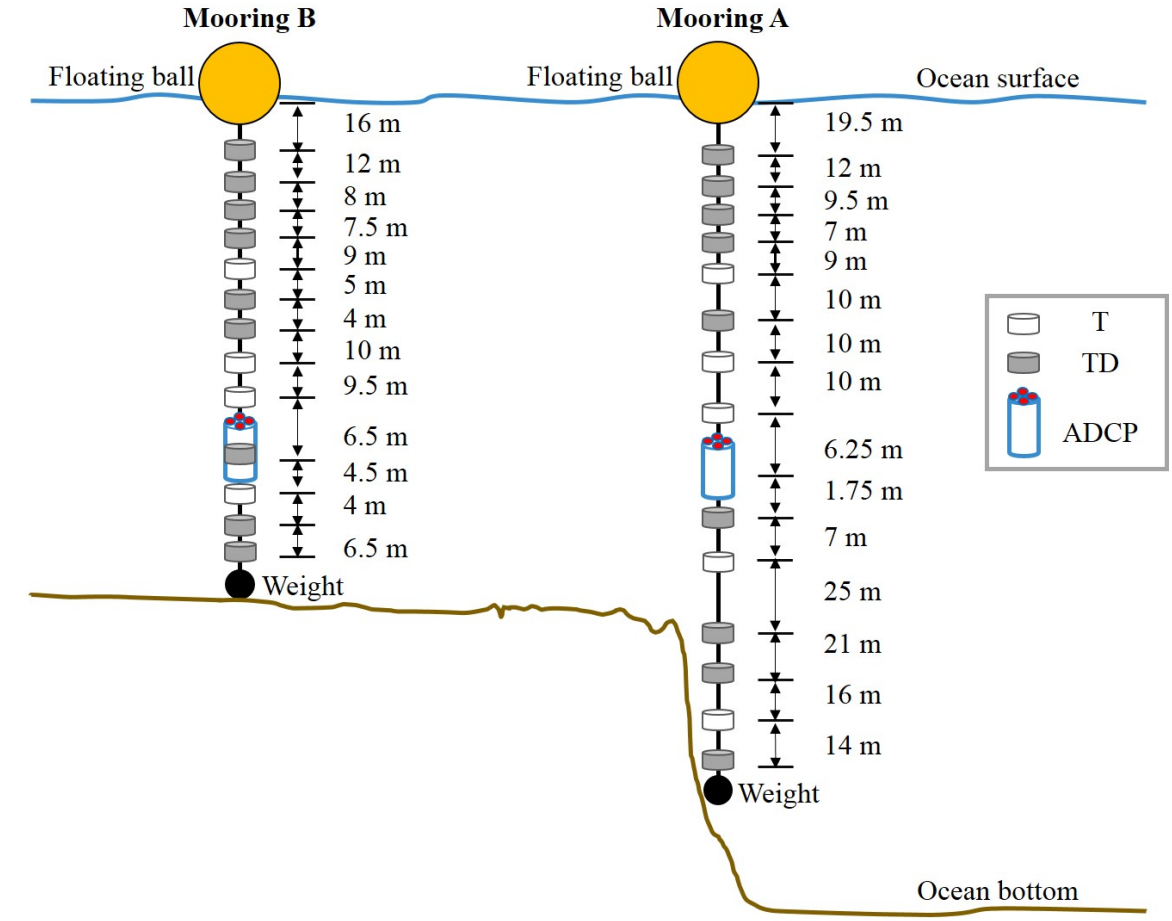

Figure 2. Mooring configuration. The T represents the temperature sensor while the TD represents the temperature and pressure sensor. The ADCP represents the upward-looking acoustic Doppler current profiler mounted in a stainless-steel frame. At mooring B, a TD is attached to the steel frame of the ADCP to measure the water temperature and pressure.

The ADCP data were available over the depth of 12 m to 78 m. To extract the current variation associated with the internal tide passage at the continental slope and NLIW passage at the mid-continental shelf, the ADCP data were smoothed with a fourth-order Butterworth filter at a cut-off frequency of 4 hours at mooring A and a bandpass frequency of 20 mins-6 hours at mooring B. The coordinates of the current data were then rotated clockwise so that the u component of velocity is along the wave propagation and positive to the southeast, and the v component of velocity is across the wave propagation and positive to the northeast. The time series of measured temperatures at moorings A and B were processed with 4-hour and 20-minute low-pass fourth-order Butterworth filters, respectively, to remove the noise and retain the information related to internal waves.

2.2 Satellite data

Close to the time when the mooring measurements conducted, one SAR image (Figure 3a) was acquired by the Gaofen-3 (GF-3) and one optical image (Figure 3b) was acquired by Moderate Resolution Imaging Spectroradiometer (MODIS) Aqua. Technical specifications of the two images are listed in Table 1. The two satellites capture the significant signatures of NLIWs on the northern continental shelf south of Hainan Island (indicated by the red arrows in Figures 3a and 3b). The observed NLIWs occur in the neap tidal period when the local barotropic tides are very weak (Figure 3c).

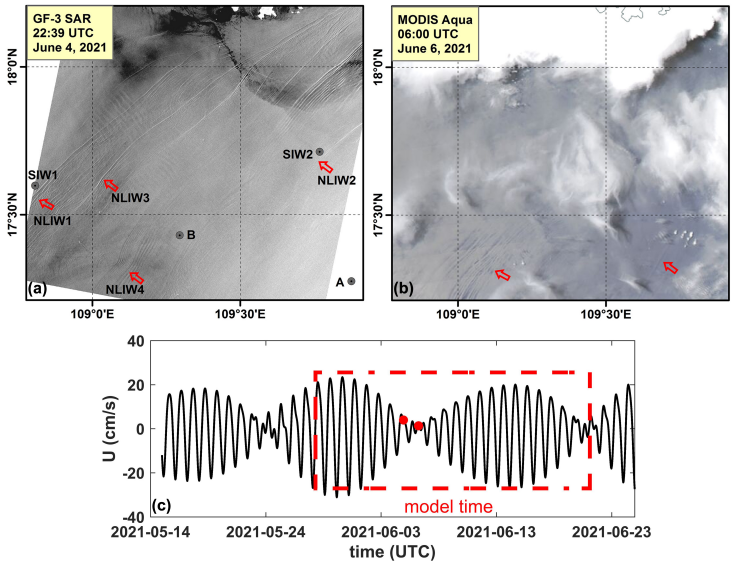

Figure 3. (a) GF-3 SAR image acquired at 22:39 UTC on June 4, 2021. (b) MODIS Aqua image acquired at 06:00 UTC on June 6, 2021. The red arrows indicate the wavefront of NLIWs observed on the northern continental shelf south of Hainan Island. The four grey points denote the locations of moorings (A and B) and simulated NLIWs (SIW1 and SIW2) in the numerical simulations. (c) Variation of local barotropic tidal current velocity from May 15 to June 25, 2021. The velocity data are derived from the tidal model of China Seas & Indonesia 2016 (Egbert and Erofeeva, 2002) at the mooring A and have been projected to the propagation direction of the internal wave observed on the images. The red points in panel (c) indicate the local barotropic tidal phase at the acquisition time of the two satellite images (a) and (b). The red dashed box covers the model time of the numerical simulations. Positive velocity indicates flow to the southeast (offshore).

Table 1. Technical Specifications of the Satellite Data Acquired in the Study

Satellite	Acquisition time (UTC)	Imaging mode	Pixel size (m)
GF-3 SAR	22:39 UTC on June 4, 2021	Fine stripmap II	10
MODIS Aqua	06:00 UTC on June 6, 2021	/	250

2.3 Numerical model

The two-dimensional (2D), nonlinear, non-hydrostatic Massachusetts Institute of Technology general circulation model (MITgcm) is applied to simulate the generation and propagation process of NLIWs on the northern continental shelf south of Hainan Island. With MITgcm a standard (EN1) and four sensitivity simulations (EN2, EN3, EN4 and EN5) were built in the study. The setups of the five simulations are summarized in Table 2.

Table 2. Setups of Numerical Simulations

Experiment	Model topography	Simulated NLIW	Experiment type
EN1	Transect I	NLIW1	Standard Experiment
EN2	Transect I without Xisha Islands	NLIW1	Sensitivity Experiment
EN3	Transect I without shelf break	NLIW1	Sensitivity Experiment
EN4	Transect II	NLIW2	Sensitivity Experiment
EN5	Transect II without Xisha Islands	NLIW2	Sensitivity Experiment

EN1 is setup to simulate the generation of the NLIW1 observed on the GF-3 SAR image (Figure 3a). EN2 and EN3 are sensitivity experiments to examine the role of continental shelf break and Xisha Islands in the generation of NLIW1. Experiment EN4 is expected to explore the multiple potential sources for generating the NLIWs, which is thus designed to reproduce the generation of the SAR-observed NLIW2 in Figure 3a. Sensitivity experiment EN5 is setup the same as EN4 except for the model topography excluding the Xisha Islands to study the source of NLIW2 by comparing with EN4. We selected the transects (I and II, red and blue lines in Figure 1) along the propagation direction of the simulated waves as the model domain. The transect I across NLIW1 passes through the moorings A and B. The transect II across NLIW2 passes through an area of the Xisha Islands where the body force for the K_1 tidal constituent in summer has a maximum force of 1.47 m^2s^{-2} (see Figure 6a of Jia et al., 2021).

The model configuration is a two-dimensional X-Z domain with a zonal length of approximately 925 km in the five simulations. The positive direction of the X-axis is opposite to the propagation direction of the simulated waves, and the Z-axis points vertically upward. As the experiments aim to model the high-frequency NLIWs, a horizontal grid size of 25 m was chosen in the middle domain, increasing to 5 km at each lateral boundary. The vertical grid resolution was 5

m in the upper 300 m, 10 m in the middle 300 m, 20 m in the lower 600 m, and 40 m in the bottom 400 m. The time step was set to 4 s to satisfy the Courant-Friedrichs-Lewy (CFL) condition. Moreover, the Richardson number-dependent parameterizations of turbulent closure (Pacanowski & Philander, 1981) were used to calculate the vertical viscosity $\nu_v = \frac{\nu_0}{(1+\alpha Ri)^n} + \nu_b$ and vertical diffusivity $\kappa_v = \frac{\nu_v}{1+\alpha Ri} + \kappa_b$, where $Ri = N^2(z)/(u_z^2 + v_z^2)$ is the Richardson number, $u(v)$ is zonal (meridional) velocity, and N is the buoyancy frequency. The parameters ν_b, κ_b, α, n and ν_0, as well as the horizontal viscosity ν_h and diffusivity κ_h, were same as those detailed in Jia et al. (2021), where $\nu_b = 1.0 \times 10^{-5}\ m^2 s^{-1}$, $\kappa_b = 1.0 \times 10^{-5}\ \mathrm{m}^2 s^{-1}$, $\alpha = 5$, $n = 1$, $\nu_0 = 1.0 \times 10^{-1}\ m^2 s^{-1}$, ν_h=$1.0 \times 10^{-2}\ \mathrm{m}^2 s^{-1}$ and κ_h=$1.0 \times 10^{-5}\ \mathrm{m}^2 s^{-1}$.

The model topography data were extracted from the GEBCO_2020 data set with a resolution of 15 arc seconds. The red lines in Figure 4 depict the profiles of the used bathymetry in the model simulations.

The initial stratification in the model was set to be horizontally uniform, and its data were taken from a combination of CTD collected data and SCS physical oceanographic data set-SCSPOD14 (Zeng et al., 2016) for June. Figure 5 shows the merged temperature and salinity profile used in the model.

The model was initialized from rest and was driven by a 24-day time series of the barotropic tidal velocities with substantial spring-neap tidal variability. The tidal forcing was constructed from the tidal model of China Seas & Indonesia 2016 from May 28, 2021 to June 21, 2021 (Figure 3c), and projected to the propagation direction of the simulated waves. In addition, to allow for the inward propagation of the tidal barotropic waves while damping the outward-propagating baroclinic waves, a sponge layer over 32 cells following Lavelle and Thacker (2008) was employed in the model.

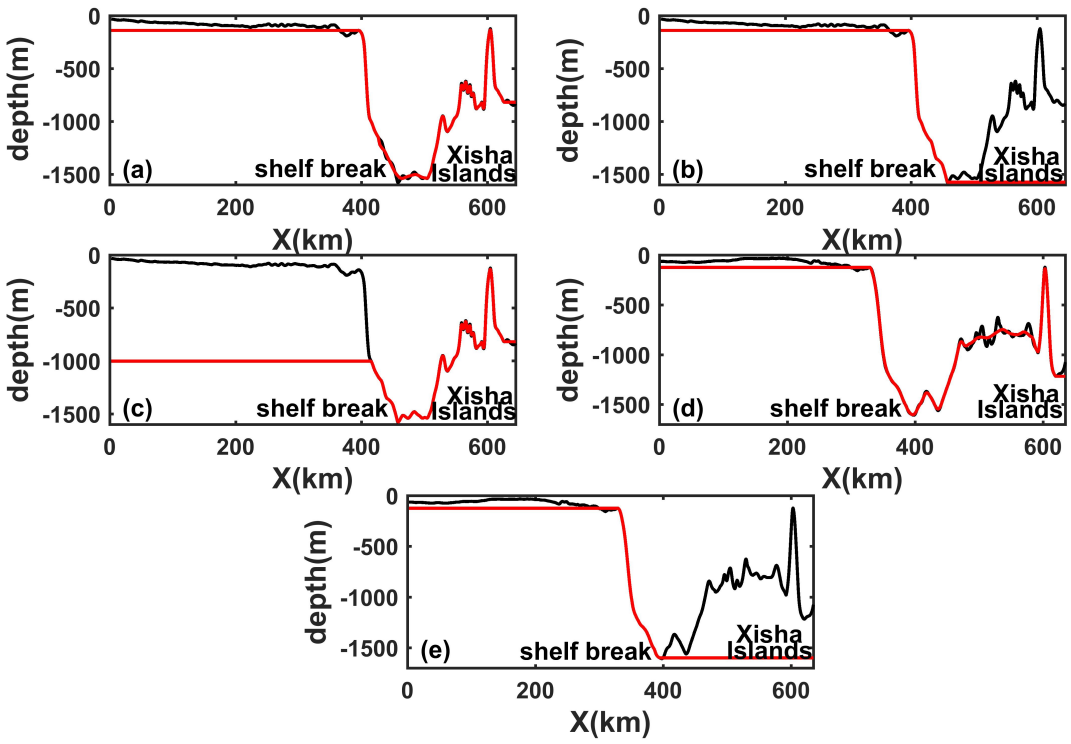

Figure 4. The bathymetry profiles used in the simulations EN1 (a), EN2 (b), EN3 (c), EN4 (d) and EN5 (e). The red line in each panel represents the topography used for the numerical simulation. The black lines in panels (a)-(c) and (d)-(e) represent the actual bathymetry (GEBCO_2020 data set) along the transect I (red line in Figure 1) and transect II (blue line in Figure 1), respectively.

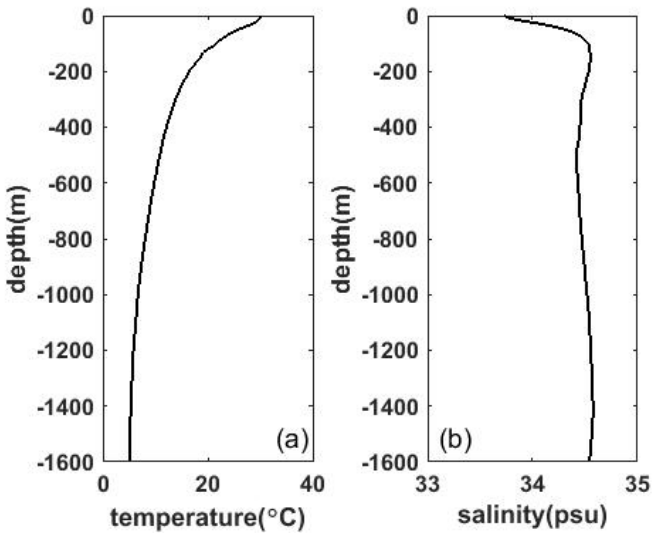

Figure 5. Initial temperature (a) and salinity (b) profiles used in the model.

2.4 Internal tide energy flux

We calculated the depth-integrated internal tide energy flux using the modeled instantaneous density and velocity profiles to quantify the baroclinic energy field on the continental shelf and deep sea. Following Nash et al. (2005), the depth-integrated internal tide energy flux is adequately approximated by the linear, hydrostatic contribution:

$$F_E = \int_{-H}^{0} \left\langle \mathbf{u}' p' \right\rangle \mathrm{dz} \quad (1)$$

where H is the total water depth, $\mathbf{u}'$ and p' are the internal wave-induced baroclinic perturbations in velocity u and pressure p. The bold variable indicates a vector quantity throughout the paper. $\langle \bullet \rangle$ denotes the average over a wave period.

The pressure perturbation $p'(z,t)$ is the instantaneous pressure $p(z,t)$ plus the surface pressure $p_{\mathrm{surf}}(t)$:

$$p'(z,t) = p(z,t) + p_{\mathrm{surf}}(t) \quad (2)$$

where the instantaneous pressure $p(z,t)$ is calculated from the density anomaly $\rho^{'}(z,t)$:

$$p(z,t) = \int_z^0 g\rho^{'}(z,t)dz \quad (3)$$

here the $\rho^{'}(z,t)$ is defined by:

$$\rho^{'}(z,t) = \rho(z,t) - \overline{\rho}(z) \quad (4)$$

where $\rho(z,t)$ is the instantaneous modeled density profile and $\overline{\rho}(z)$ is the time mean density.

$p_{\mathrm{surf}}(t)$ is calculated through the baroclinicity condition:

$$p_{\mathrm{surf}}(t) = -\frac{1}{H}\int_{-H}^0 p(z,t)\mathrm{dz} \quad (5)$$

The velocity perturbation $\mathbf{u}^{'}(z,t)$ is calculated as the instantaneous horizontal velocity $\mathbf{u}(z,t)$ minus the temporally averaged velocity $\overline{\mathbf{u}_z}(z)$ and the temporally varying barotropic velocity $\overline{\mathbf{u_0}}(t)$:

$$\mathbf{u}^{'}(z,t) = \mathbf{u}(z,t) - \overline{\mathbf{u}_z}(z) - \overline{\mathbf{u_0}}(t) \quad (6)$$

where the $\overline{\mathbf{u_0}}(t)$ is determined from the baroclinicity condition:

$$\overline{\mathbf{u_0}}(t) = \frac{1}{H}\int_{-H}^0 [\mathbf{u}(z,t) - \overline{\mathbf{u}_z}(z)]\,\mathrm{dz} \quad (7)$$

3 Results

3.1 Internal wave characteristics inferred from in situ and satellite observation

In this sub-section, the characteristics of the internal waves on the northern continental shelf south of Hainan Island were described based on the in situ and satellite observations. Figure 6 shows the temperature and velocity observation data series at mooring A. Significant quasi-diurnal oscillations of isotherm from June 1 to June 3, 2021 can be seen in Figure 6a, in which the largest vertical amplitude exceeded 15 m. The oscillations suggest that energetic first-

mode diurnal internal tides existed in the ocean from June 1 to June 3, 2021. Synchronous velocity observation data (Figure 6b) suggest that these observed internal tides propagated shoreward. In addition to the dominant component of diurnal internal tides, some high-frequency waves of 40-60 min duration and 2-7 m amplitude are seen in Figure 6a, which ride on trough of the diurnal internal tide. We do not focus on these high-frequency, small-amplitude waves in the study. The local barotropic tidal current weakened significantly from June 1 to June 3, as shown in Figure 3c. However, no weakening trend was found in the amplitude of the observed shoreward internal tides during the three days (Figure 6a), suggesting that the local barotropic tidal currents did not dominate the generation of the shoreward internal tides. Moreover, the satellite observation (Figure 3) captured the NLIWs when local barotropic tidal currents were very weak. A reasonable explanation for the occurrence of internal waves irrelevant to the local barotropic tidal current is that the Xisha Islands play a more critical role in generating the observed internal waves than the shelf break, as inferred in our previous study (Jia et al., 2021).

In addition to the dominance of remote generation wave sources, multiple sources are revealed by the in situ and satellite observations. The NLIW packets observed on the GF-3 SAR image (e.g., the NLIW1, NLIW2, NLIW3 and NLIW4 in Figure 3a) exhibit slightly different geographic distributions and propagation directions. Furthermore, the separation distance between two consecutive NLIW packets (e.g., the NLIW1 and NLIW3) disagrees with the tidal cycle. These diverse features regarding the geographic distribution, propagation direction and separation distance are not in accordance with a single tidal origin, suggesting the existence of multiple source sites in the region. Field observation at the mid-continental shelf (mooring B) provides further supports for such a possibility. For example, the measured temperature series on June 4 (Figure 7) show that NLIWs on the day were observed at least three times (indicated by the black arrows) and not spaced by a regular tidal cycle, which could be the result of a combination of NLIWs from multiple sources.

In summary, the in situ and satellite observations suggest that the NLIWs observed on the northern continental shelf south of Hainan Island are remotely generated by the Xisha Islands and multiple sources exist in the Xisha Islands. In the next section, the remote generation process and multiple sources of NLIWs are elucidated by the 2D numerical simulations with the MITgcm.

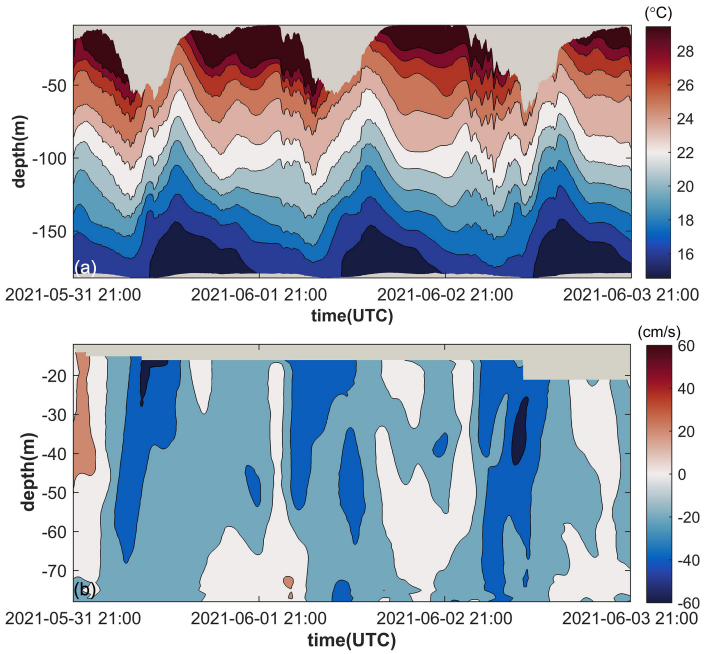

Figure 6. Depth-time series of measured temperature (a) and baroclinic velocity (b) at the mooring A from 21:00 UTC on May 31, 2021 to 22:14 UTC on June 3, 2021. Positive velocity indicates flow to the southeast (offshore).

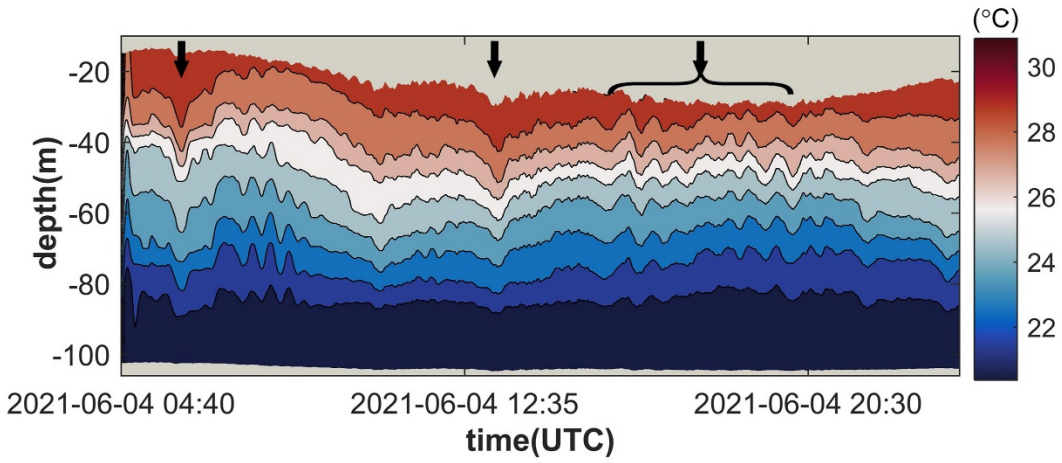

Figure 7. In situ temperature measurements from 04:00 UTC on June 4, 2021 to 00:00 UTC on June 5, 2021 at the mooring B. The vertical black arrows indicate the NLIWs identified in the field measurement.

3.2 Generation of the internal waves inferred from numerical simulation

In this sub-section, five 2D numerical simulations were performed to illustrate the remote generation process of NLIWs on the northern continental shelf south of Hainan Island. Details of the model setups can refer to Section 2.3.

3.2.1 Validation of standard simulation

The standard simulation EN1 is compared to mooring measurement and SAR observation in three ways to demonstrate how well the different metrics obtained from the model match the mooring and satellite observation.

A comparison between the modeled and observed across-shelf barotropic currents at mooring A is depicted in Figure 8. The observed currents were obtained by averaging the measured velocity data, which extended from -12 m to -78 m. Superimposed over this are the predicted barotropic currents (averaged over the same depth) from standard simulation EN1. The overall match in the variation of the barotropic currents confirms the exact simulation of the standard experiment, although the predicted slightly underpredicts the barotropic currents at the negative peak. The underprediction is likely due to the underresolved bathymetry in the 2D model which does not reproduce the strength or the complexity of the currents around the mooring.

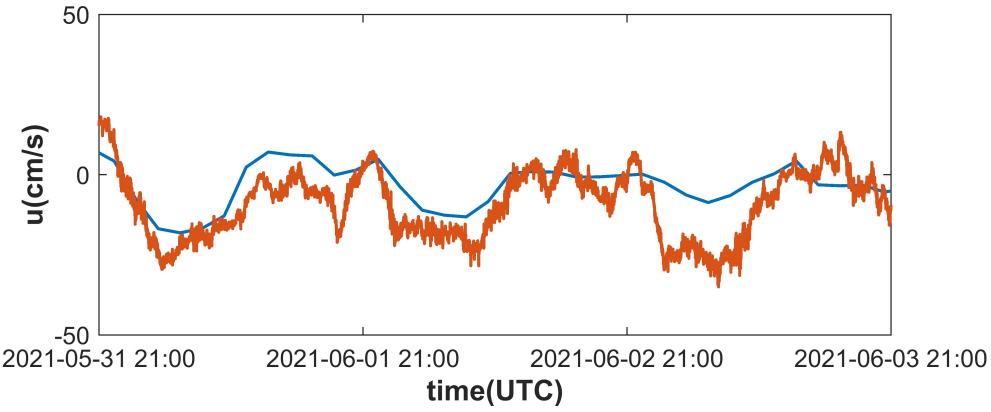

Figure 8. Comparison of modeled (blue line) and observed (red line) across-shelf barotropic currents at mooring A from May 31 to June 3, 2021. Positive velocity indicates flow to the southeast.

Moreover, Figure 9 presents the simulated displacement of 25.5°C isotherms (representing the thermocline) in EN1 at the mooring A. On the one hand, the simulated thermocline amplitude in EN1 is not completely in-phase with the local barotropic tide (Figure 3c) during the simulation period. On the other hand, their magnitude is 17 m from June 1 to June 3. The two aspects are both consistent with the in situ and satellite observations presented in section 3.1.

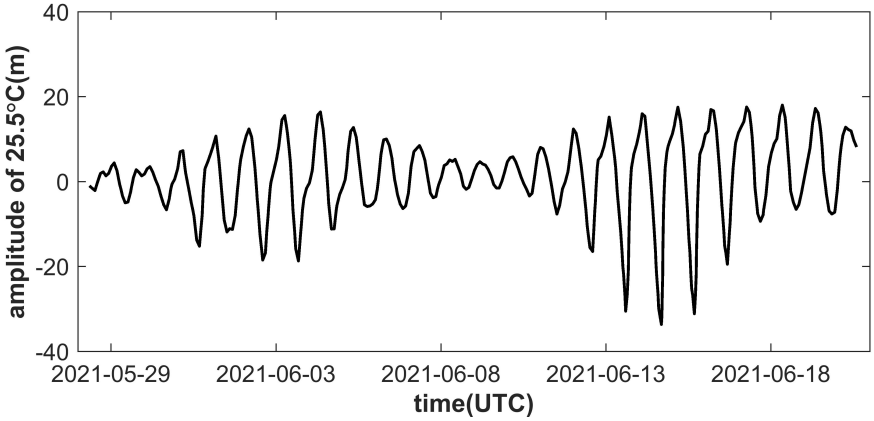

Figure 9. Displacement of 25.5°C isotherms (representing the thermocline) in the standard simulation EN1 at the mooring A.

Besides, we compare our simulated NLIWs to the SAR imagery (Figure 3a) to demonstrate the accuracy of EN1. The time for the SAR observation is referred to T. Figure 10 displays the model results of EN1 at time T. We note that a packet of NLIWs (denoted as SIW1, marked in black arrow in Figure 10a) appears at the mid-continental shelf. The SIW1 is very close to the SAR-observed NLIW1 as shown in Figure 3a. Moreover, the leading two solitons in modeled SIW1 are spaced by approximately 1.2 km, consistent with the distance of the leading two solitons in observed NLIW1 of 1.15 km.

Overall, the above comparisons demonstrate the standard model's capability to correctly simulate the generation of NLIWs on the northern continental shelf south of Hainan Island.

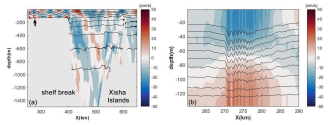

Figure 10. (a) Numerical simulations of the baroclinic horizontal velocity field overlain with isotherms taken at time T (GF-3 SAR acquisition time) in the standard simulation EN1. (b) Closeup of the fragment depicted by the red rectangle of the panel (a). Shaded color represents the horizontal baroclinic velocities, and black lines represent contour plots of temperature. The black arrow points to the modeled internal wave SIW1. Positive velocity indicates flow to the southeast.

3.2.2 Internal tidal beam mechanism

Preliminary theoretical analyses (Jia et al., 2021) have suggested that the NLIWs on the northern continental shelf south of Hainan Island are excited by the interaction of the diurnal internal tidal beam from Xisha Islands and pycnocline. In the sub-section, the remote generation process is further investigated by the numerical simulations of EN1-EN3.

Figure 11 shows the temperature distributions at Z=-47 m (representing the

thermocline) on the X-T (Time) plane for simulations EN1 and EN2. Upward intermittent fluctuations on the X-T plane (Figure 11a, inset), which indicate the formation of NLIWs, are present in simulation EN1 (Figure 11a) but not in EN2 (Figure 11c). That confirms that Xisha Islands are the source of the NLIWs. SIW1 is the NLIW simulated in EN1 corresponding to the NLIW1 observed on the GF-3 SAR image (Figure 3a). Tracking the propagation of the simulated SIW1 (dashed green line in Figure 11a) suggests it evolving from the interfacial internal wave at the time T-64 h (indicated by the dashed black line in Figure 11a). From the location of the interfacial wave to Xisha Islands, no significant shoreward interfacial wave motion (interfacial internal tide) is found at Z=-47 m in EN1 (Figure 11a). Besides, the location of the interfacial internal wave at the time T-64 h (indicated by the black arrows in Figure 12) is consistent with the intersecting point of the near-surface pycnocline and the diurnal internal tidal beam from Xisha Islands in simulation EN3 (characterized by the narrow slanting bands of elevated velocities in Figure 12b, whose ray path is indicated by the dashed red line). So, we suggest that the interfacial internal wave observed at the time T-64 h in EN1 is triggered by the internal tidal beam from Xisha Islands. Moreover, in simulation EN3 with only the Xisha Islands considered, only interfacial internal waves (but no NLIWs) are generated. This suggests that the transformation of interfacial internal waves to NLIWs in EN1 is related to the abrupt shoaling bottom topography of shelf break which strengthens the nonlinearity of the interfacial internal wave.

In summary, the simulation results of EN1-EN3 demonstrate that the NLIWs on the northern continental shelf south of Hainan Island can form from a two-stage process: first, the beam from Xisha Islands interacts with the pycnocline and gives rise to a shoreward interfacial wave, and second, as the interfacial wave propagates onto the continental shelf, it evolves through nonlinear transformation into a packet of NLIWs. This process is in line with the generation of NLIWs in the moderate strong thermocline proposed by Gerkema (2001).

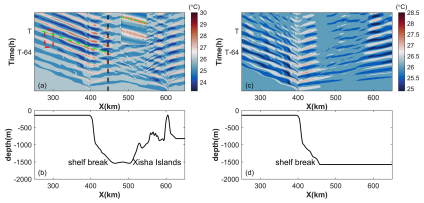

Figure 11. The upper panels are contour plots of the temperature (°C) at Z=-47 m in the X-T plane for EN1 (a) and EN2 (c). The inset in (a) is a local enlargement of the dashed red box. The dashed green line indicates the propagating of simulated shoreward SIW1. The dashed black line represents the position of the internal interfacial wave. The lower panels are the model topography used in EN1 (b) and EN2 (d).

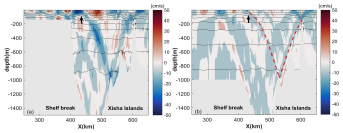

Figure 12. Numerical simulations of the baroclinic horizontal velocity field overlain with isotherms taken at time T-64 h for standard simulation EN1 (a) and sensitivity simulation EN3 (b). Shaded color represents the horizontal baroclinic velocities, and black lines represent contour plots of temperature. The black arrow points to the modeled internal wave SIW1. The red dashed line represents the ray path of K_1 internal tide from Xisha Islands, which is calculated according to the formula (2) of Liang et al. (2019).

3.2.3 Effects of locally generated internal tides

LITs are radiated away from the shelf break with a critical slope. Figure 13 shows the wave beams in simulation EN2 with only the continental shelf break considered. It suggests that the continental shelf break forms a shoreward (solid magenta line) and two seaward beams (dashed magenta lines). These beams are reflected multiple times at the ocean surface and bottom. The question then arises as to whether the shoreward and seaward LITs interact with the incident RITs and thereby affect the generation of NLIWs on the northern continental shelf south of Hainan Island.

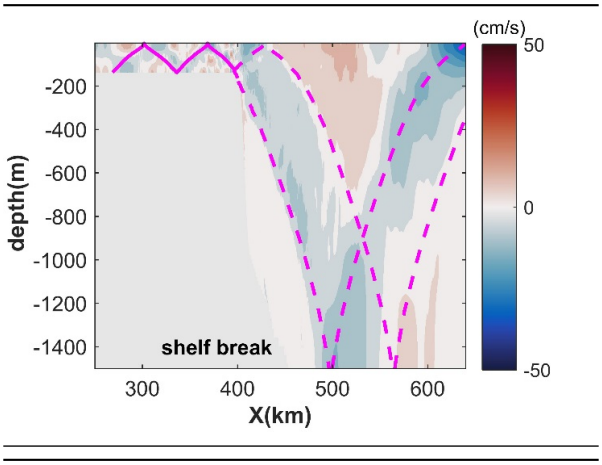

Figure 13. Baroclinic horizontal velocity overlapped with theoretical beams (magenta lines) in simulation EN2. The solid and dashed magenta lines represent the onshore and offshore beams emanating from the continental shelf break, respectively.

To quantify the effect of the shoreward LITs on the generation of NLIWs, the depth-integrated internal tide energy flux is calculated on the mid-continental shelf in simulations EN1, EN2 and EN3, respectively. When the model topography only includes the Xisha Islands (or continental shelf break), the energy flux on the mid-continental shelf is only associated with the RITs (or LITs). As illustrated in Figure 14, the RIT-related energy flux (Figure 14c) shows a comparative agreement with the net internal flux caused by the interaction of

shoreward LITs and RITs (Figure 14a), and its magnitude is approximately 71% of the magnitude of net energy flux. Thus, the RITs are the principal baroclinic energy source on the shelf. In contrast, shoreward LIT-related energy flux (Figure 14b) is very weak, less than 16% of the net energy flux, suggesting that the shoreward LITs hardly contribute to the internal tide energy flux on the shelf. Moreover, no NLIWs are generated in the simulation only considering the continental shelf. Therefore, the generation of NLIWs on the shelf is almost unaffected by the shoreward LITs.

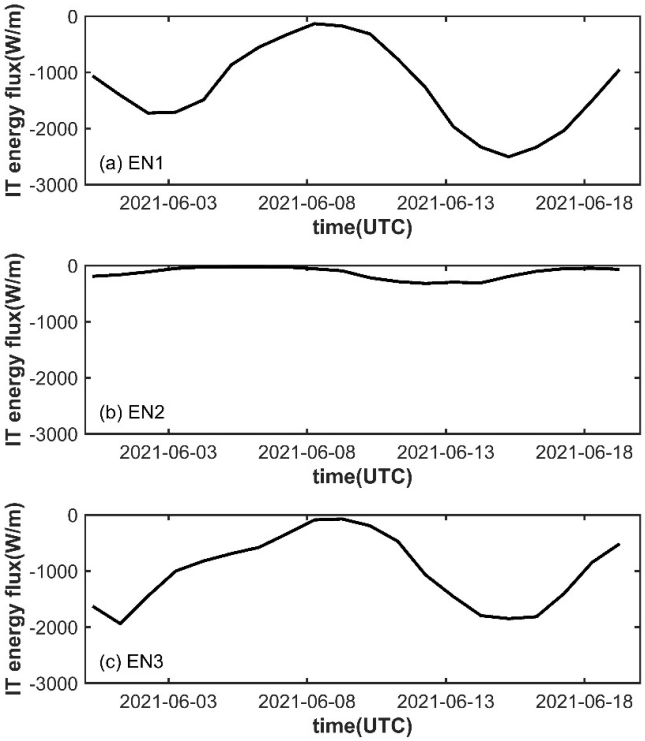

Figure 14. Depth-integrated internal tide (IT) energy flux calculated on the mid-continental shelf in simulations EN1 (a), EN2 (b) and EN3 (c). Positive energy flux indicates transport to the southeast (offshore).

To examine the effects of seaward LITs in the deep sea, the depth-integrated internal tide energy flux is calculated on the continental slope east of the critical topography in simulations EN1, EN2 and EN3 (Figure 15). The net energy flux east of the critical point in EN1 (Figure 15a) is mostly directed offshore and

behaves a similar pattern to the seaward LIT-related energy flux (Figure 15b). Comparatively, the RIT-related energy flux east of the critical point (Figure 15c) is always directed onshore, indicating that the baroclinic energy field in the deep sea is controlled by the seaward LITs instead of the RITs.

In summary, the LITs play an important role in the deep sea while their effects on the shelf can be negligible. On the shelf, the baroclinic energy is dominated by the incident RITs which thereby is the generation source of the NLIWs.

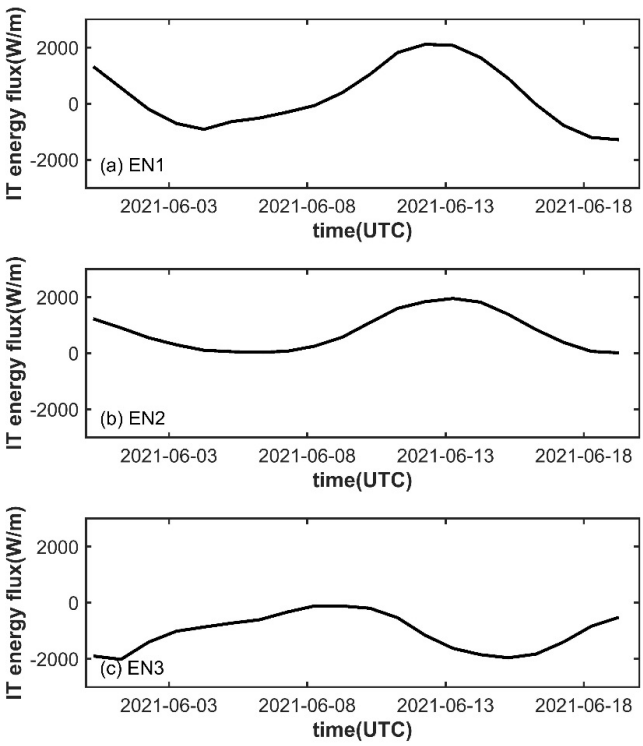

Figure 15. Depth-integrated internal tide (IT) energy flux calculated east of the critical continental slope in simulations EN1 (a), EN2 (b) and EN3 (c). Positive energy flux indicates transport to the southeast (offshore).

3.2.4 Multiple remote sources and mechanisms

To confirm the existence of multiple remote wave sources, simulation EN4 was set with nearly realistic ocean environment to reproduce the generation of the

NLIW2 on the SAR image (Figure 3a), whose result is then compared to the sensitivity experiment EN5 with only the continental shelf break considered.

Figures 16a and c show the temperature distributions at Z=-47 m between the continental shelf and Xisha Islands for simulations EN4 and EN5, respectively. Their zoomed-in views are shown in Figures 16b and d. In EN5 (Figures 16c and d), linear internal wave radiates upward from the shelf break onto the shelf (westward of X=331 km) in each tidal cycle. The propagation of the linear internal wave follows closely to the characteristics given by the theoretical speed of the first-mode linear internal tide from the shelf break (dashed magenta lines in Figures 16c and d), indicating that the source of linear internal wave is the local shelf break. In EN4 (Figures 16a and b), a similar linear internal wave appears on the shelf in each tidal cycle until T-58 h; however, after T-58h it appears more like a soliton. Two examples of such soliton are surrounded by the solid blue lines in Figure 16b. The transform from the locally generated linear internal wave to a soliton is possibly due to the enhanced nonlinearity caused by the onshore internal tide energy flux from Xisha Islands (Figure 14c). Next to each soliton in simulation EN4, another NLIW train appears on the shelf. Two examples of NLIW trains are surrounded by the solid yellow lines in Figure 16b. The propagation of the NLIW train in EN4 is consistent with the theoretical characteristic curve for the first-mode linear internal tide from Xisha Islands (dashed green lines in Figures 16a and b). Considering that there is no NLIW train in EN5, we suggest the NLIW train in EN4 is generated by the interfacial internal tide from Xisha Islands.

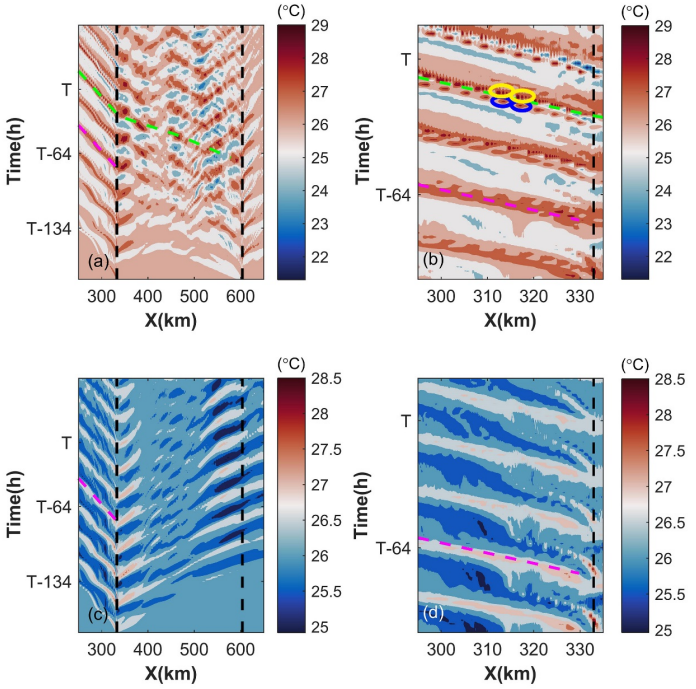

Figure 16. Distributions of temperature at Z=-47 m between the continental shelf and Xisha Islands for simulations EN4 (a) and EN5 (c). (b) and (d) are the zoomed-in views of the panels (a) and (c), respectively. The dashed black vertical lines represent the positions of shelf break and Xisha Islands. The dashed green and magenta slanting lines are the characteristic lines following the theoretical speed of the first-mode linear internal tide from the Xisha Islands and continental shelf break, respectively. Two examples of soliton and NLIW train simulated in EN4 are surrounded by the solid blue and yellow lines in panel (b), respectively.

The generation mechanism of internal tides can be determined using the normalized tidal excursion parameter (Buijsman et al., 2010). The excursion parameter

is around 0.12 in the ridge of the Xisha Islands in EN4, suggesting that the internal waves in EN4 are generated more in the mixed tidal lee wave regime. In the mixed tidal lee wave regime, first-mode internal waves in the forcing frequency are mainly excited while linear internal tide beams are not well developed. Under the influence of nonhydrostatic and rotational dispersion in the far field, the first-mode internal waves can disintegrate into strong NLIW trains, as our simulation of Figures 16a and b shows.

At time T, the simulated NLIW in EN4 (denoted as SIW2, marked in black arrow in Figure 17a) is very close to the SAR-observed NLIW2 (Figure 3a), confirming the Xisha Islands via the mixed tidal lee wave regime as a source for the NLIWs on the northern continental shelf south of Hainan Island. Given that the NLIWs in simulation EN1 arise from another sill in Xisha Islands via an internal tidal beam mechanism, we suggest more than one source and mechanism in Xisha Islands to generate the NLIWs on the shelf.

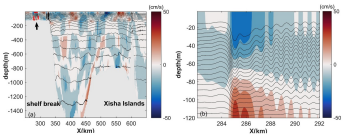

Figure 17. (a) Numerical simulations of the baroclinic horizontal velocity field overlain with isotherms taken at time T in the simulation EN4. (b) Closeup of the fragment depicted by the dashed red box of panel (a). Shaded color represents the horizontal baroclinic velocities, and black lines represent contour plots of temperature. The black arrow points to the modeled internal wave SIW2. Positive velocity indicates flow to the southeast.

4 Discussion

The northern continental shelf south of Hainan Island in the northwestern SCS is home to many vigorous NLIW motions; however, the generation of these NLIWs remain less well-understood compared to those in other continental shelves and coastal oceans, such as the northeastern SCS (Alford et al., 2015; Davis et

al., 2020) and Andaman Sea (Cai et al., 2021; Osborne & Burch, 1980). Our previous study (Jia et al., 2021) based on SAR observation and theoretical analysis suggested that these NLIWs on the northern continental shelf south of Hainan Island source from Xisha Islands via the internal tidal beam mechanism. In the study, a combination of satellite observation, in situ measurement and 2D numerical simulation with MITgcm provides solid support for the proposed remote generation process. It enhances our understanding of the diverse and complicated generation of NLIWs in the study area.

Apart from the RITs coming from Xisha Islands, LITs emanating from the shelf break are also part of the baroclinic tide energy field around the continental shelf. The internal tide energy flux (Figure 14) shows that the LITs have an almost negligible interference of incident RITs and subsequent NLIW generation on the mid-shelf. The slight increase in internal tide energy flux at the mid-shelf area in the simulation with the continental shelf break considered (Figure 14a compared to Figure 14c) is mainly due to the amplified amplitude and energy of RITs as they propagate and steepen up the shelf.

Complicated oceanic bottom topography and hydrological environment allow for more than one generation source and mechanism of internal waves in the Xisha Islands. Our two separate 2D simulations with the realistic topography and tidal forcing both show a comparative agreement with the SAR observation (Figure 3a), thus revealing that the NLIWs on the northern continental shelf south of Hainan Island can be generated from different sills in the Xisha Islands via the internal tidal beam or mixed tidal lee wave regime. In the future, a three-dimensional numerical simulation combined the satellite observation could elucidate how many sources and mechanisms in Xisha Islands give rise to the NLIWs on the continental shelf.

5 Conclusions

The generation of NLIWs on the northern continental shelf south of Hainan Island is investigated through a synergistic analysis of satellite observations, in situ measurements and numerical simulations in the study. The main conclusions draw below:

1. A diurnal internal tidal beam emanating from Xisha Islands interacts with the pycnocline and initiates the NLIWs observed on the continental shelf.
2. Locally generated shoreward internal tides emanating from the continental shelf break have little effect on the generation of NLIWs on the shelf.
3. Various sources and mechanisms in Xisha Islands can excite the generation of NLIWs on the shelf.

Combined with our previous study (Jia et al., 2021), this study makes a significant step toward a comprehensive understanding of the NLIW dynamics on the continental shelf south of Hainan Island in the SCS. The study is based on a 2D numerical model. To reproduce all details of the internal wave structure south

of Hainan Island, the precise three-dimensional numerical simulations will be conducted in the future study.

Acknowledgments

The authors are grateful to the following people who have provided valuable assistance in the operation, deployment and recovery of the in situ instruments: Mr. Yuan Lu from the Qingdao Ziwu Navigation Technology Co., Ltd. and Dr. Yongzheng Ren, Dr. Jin Sha, Ms. Ke Wu, Mr. Ning Wang, and Ms. Nannan Zi from the Aerospace Information Research Institute, Chinese Academy of Sciences. The authors also thank the NASA for providing the MODIS Aqua data and the National Satellite Ocean Application Service for providing the GF-3 SAR data. The study was supported by grants from the National Science Foundation of China project (41876201) and National Science Fund for Distinguished Young Scholars (42025605).

Data Availability Statement

The SCSPOD14 data were downloaded from http://dx.doi.org/10.6084/m9.figshare.c.1513842, the GEBCO_2020 data were downloaded from https://www.gebco.net/data_and_products/gridded_bathyme and the tidal solutions of China Seas & Indonesia 2016 were downloaded from https://www.tpxo.net/regional/.

References

Alford, M. H., Peacock, T., MacKinnon, J. A., Nash, J. D., Buijsman, M. C., Centuroni, L. R., et al. (2015). The formation and fate of internal waves in the South China Sea. *Nature*, *521*(7550), 65-69. doi:10.1038/nature14399

Alpers, W. (1985). Theory of radar imaging of internal waves. *Nature*, *314*(6008), 245-247.

Apel, J. R., Badiey, M., Chiu, C. S., Finette, S., Headrick, R., Kemp, J., et al. (1997). An overview of the 1995 SWARM shallow-water internal wave acoustic scattering experiment. *IEEE Journal of Oceanic Engineering*, *22*(3), 465-500. doi:10.1109/48.611138

Buijsman, M. C., Kanarska, Y., & McWilliams, J. C. (2010). On the generation and evolution of nonlinear internal waves in the South China Sea. *Journal of Geophysical Research: Oceans*, *115*. doi:10.1029/2009JC005275

Cai, S., Wu, Y., Xu, J., Chen, Z., Xie, J., & He, Y. (2021). On the generation and propagation of internal solitary waves in the southern Andaman Sea: A numerical study. *Science China Earth Sciences*, *64*(10), 1674-1686. doi:10.1007/s11430-020-9802-8

Cole, S. T., Rudnick, D. L., Hodges, B. A., & Martin, J. P. (2009). Observations of tidal internal wave beams at Kauai Channel, Hawaii. *Journal of Physical Oceanography*, *39*(2), 421-436. doi:10.1175/2008JPO3937.1

Davis, K. A., Arthur, R. S., Reid, E. C., Rogers, J. S., Fringer, O. B., DeCarlo, T. M., & Cohen, A. L. (2020). Fate of internal waves on a shallow shelf. *Journal*

of Geophysical Research: Oceans, *125*(5). doi:10.1029/2019JC015377

Duda, T. F., & Preisig, J. C. (1999). A modeling study of acoustic propagation through moving shallow-water solitary wave packets. *IEEE Journal of Oceanic Engineering*, *24*(1), 16-32. doi:10.1109/48.740153

Egbert, G. D., & Erofeeva, S. Y. (2002). Efficient inverse modeling of barotropic ocean tides. *Journal of Atmospheric and Oceanic Technology*, *19*(2), 183-204. doi:10.1175/1520-0426(2002)019<0183:EIMOBO>2.0.CO;2

Fer, I., Koenig, Z., Kozlov, I. E., Ostrowski, M., Rippeth, T. P., Padman, L., et al. (2020). Tidally forced lee waves drive turbulent mixing along the Arctic Ocean margins. *Geophysical Research Letters*, *47*(16). doi:10.1029/2020GL088083

Fringer, O. B., Gerritsen, M., & Street, R. L. (2006). An unstructured-grid, finite-volume, nonhydrostatic, parallel coastal ocean simulator. *Ocean Modelling*, *14*(3-4), 139-173. doi:10.1016/j.ocemod.2006.03.006

Garrett, C., & Munk, W. (1979). Internal waves in the ocean. *Annual Review of Fluid Mechanics*, *11*(1), 339-369. doi:10.1146/annurev.fl.11.010179.002011

Gerkema, T. (2001). Internal and interfacial tides: beam scattering and local generation of solitary waves. *Journal of Marine Research*, *59*(2), 227-255. doi:10.1357/002224001762882646

Heathershaw, A. D. (1985). Some observations of internal wave current fluctuations at the shelf-edge and their implications for sediment transport. *Continental Shelf Research*, *4*(4), 485-493. doi: 10.1016/0278-4343(85)90006-8

Helfrich, K. R., & Grimshaw, R. H. (2008). Nonlinear disintegration of the internal tide. *Journal of Physical Oceanography*, *38*(3), 686-701. doi:10.1175/2007JPO3826.1

Huang, X., Chen, Z., Zhao, W., Zhang, Z., Zhou, C., Yang, Q., & Tian, J. (2016). An extreme internal solitary wave event observed in the northern South China Sea. *Scientific Reports*, *6*(1), 1-10. doi:10.1038/srep30041

Jackson, C. R., Da Silva, J. C., & Jeans, G. (2012). The generation of nonlinear internal waves. *Oceanography*, *25*(2), 108-123. doi:10.5670/oceanog.2012.46

Jia, T., Liang, J., Li, Q., Sha, J., & Li, X. -M. (2021). Generation of shoreward nonlinear internal waves south of the Hainan Island: Synthetic aperture radar observations and numerical simulations. *Journal of Geophysical Research: Oceans*, *126*(6). doi:10.1029/2021JC017334

Kanarska, Y., Shchepetkin, A., & McWilliams, J. C. (2007). Algorithm for nonhydrostatic dynamics in the regional oceanic modeling system. *Ocean Modelling*, *18*(3-4), 143-174. doi:10.1016/j.ocemod.2007.04.001

Klemas, V. (2012). Remote sensing of ocean internal waves: An overview.

Journal of Coastal Research, *28*(3), 540-546. doi:10.2112/JCOASTRES-D-11-00156.1

Lamb, K. G. (2014). Internal wave breaking and dissipation mechanisms on the continental slope/shelf. *Annual Review of Fluid Mechanics*, *46*, 231-254. doi:10.1146/annurev-fluid-011212-140701

Lavelle, J. W., & Thacker, W. C. (2008). A pretty good sponge: Dealing with open boundaries in limited-area ocean models. *Ocean Modelling*, *20*(3), 270-292. doi:10.1016/j.ocemod.2007.10.002

Lee, C. Y., & Beardsley, R. C. (1974). The generation of long nonlinear internal waves in a weakly stratified shear flow. *Journal of Geophysical Research*, *79*(3), 453-462. doi:10.1029/JC079i003p00453

Liang, J., Li, X. -M., Sha, J., Jia, T., & Ren, Y. (2019). The lifecycle of nonlinear internal waves in the northwestern South China Sea. *Journal of Physical Oceanography*, *49*(8), 2133-2145. doi:10.1175/JPO-D-18-0231.1

Lynch, J. F., Lin, Y. T., Duda, T. F., & Newhall, A. E. (2010). Acoustic ducting, reflection, refraction, and dispersion by curved nonlinear internal waves in shallow water. IEEE *Journal of Oceanic Engineering*, *35*(1), 12-27.

Marshall, J., Hill, C., Perelman, L., & Adcroft, A. (1997). Hydrostatic, quasi-hydrostatic, and nonhydrostatic ocean modeling. *Journal of Geophysical Research: Oceans*, *102*(C3), 5733-5752. doi:10.1029/96JC02776

Maxworthy, T. (1979). A note on the internal solitary waves produced by tidal flow over a three-dimensional ridge. *Journal of Geophysical Research: Oceans*, *84*(C1), 338-346. doi:10.1029/JC084iC01p00338

Mendes, R., Da Silva, J. C. B., Magalhaes, J. M., St-Denis, B., Bourgault, D., Pinto, J., & Dias, J. M. (2021). On the generation of internal waves by river plumes in subcritical initial conditions. *Scientific Reports*, *11*(1), 1-12. doi:10.1038/s41598-021-81464-5

Moum, J. N., Farmer, D. M., Smyth, W. D., Armi, L., & Vagle, S. (2003). Structure and generation of turbulence at interfaces strained by internal solitary waves propagating shoreward over the continental shelf. *Journal of Physical Oceanography*, *33*(10), 2093-2112. doi:10.1175/1520-0485(2003)033<2093:SAGOTA>2.0.CO;2

Nash, J. D., Alford, M. H., & Kunze, E. (2005). Estimating internal wave energy fluxes in the ocean. *Journal of Atmospheric and Oceanic Technology*, *22*(10), 1551-1570. doi:10.1175/JTECH1784.1

Nash, J. D., Kelly, S. M., Shroyer, E. L., Moum, J. N., & Duda, T. F. (2012). The unpredictable nature of internal tides on continental shelves. *Journal of Physical Oceanography*, *42*(11), 1981-2000. doi:10.1175/JPO-D-12-028.1

Osborne, A. R., & Burch, T. L. (1980). Internal solitons in the Andaman Sea. *Science*, *208*(4443), 451-460. doi:10.1126/science.208.4443.451

Osborne, A. R., Burch, T. L., & Scarlet, R. I. (1978). The influence of internal waves on deep-water drilling. *Journal of Petroleum Technology*, *30*(10), 1497-1504.

Pacanowski, R. C., & Philander, S. G. H. (1981). Parameterization of vertical mixing in numerical models of tropical oceans. *Journal of Physical Oceanography*, *11*(11), 1443-1451. doi:10.1175/1520-0485(1981)011<1443:POVMIN>2.0.CO;2

Pingree, R. D., & New, A. L. (1991). Abyssal penetration and bottom reflection of internal tidal energy in the Bay of Biscay. *Journal of Physical Oceanography*, *21*(1), 28-39. doi:10.1175/1520-0485(1991)021<0028:APABRO>2.0.CO;2

Pomar, L., Morsilli, M., Hallock, P., & Bádenas, B. (2012). Internal waves, an under-explored source of turbulence events in the sedimentary record. *Earth-Science Reviews*, *111*(1-2), 56-81. doi:10.1016/j.earscirev.2011.12.005

Quaresma, L. S., Vitorino, J., Oliveira, A., & Da Silva, J. (2007). Evidence of sediment resuspension by nonlinear internal waves on the western Portuguese mid-shelf. *Marine Geology*, *246*(2-4), 123-143. doi:10.1016/j.margeo.2007.04.019

Raju, N. J., Dash, M. K., Dey, S. P., & Bhaskaran, P. K. (2019). Potential generation sites of internal solitary waves and their propagation characteristics in the Andaman Sea-a study based on MODIS true-colour and SAR observations. *Environmental Monitoring and Assessment*, *191*(3). doi:10.1007/s10661-019-7705-8

Sandstrom, H., & Elliott, J. A. (1984). Internal tide and solitons on the Scotian Shelf: A nutrient pump at work. *Journal of Geophysical Research: Oceans, 89*(C4), 6415-6426. doi:10.1029/JC089iC04p06415

Sandstrom, H., & Oakey, N. S. (1995). Dissipation in internal tides and solitary waves. *Journal of Physical Oceanography*, *25*(4), 604-614. doi:10.1175/1520-0485(1995)025<0604:DIITAS>2.0.CO;2

Shanks, A. L. (1987). The onshore transport of an oil spill by internal waves. *Science*, *235*(4793), 1198-1200. doi:10.1126/science.235.4793.1198

Shanks, A. L. (2021). Observational evidence and open questions on the role of internal tidal waves on the concentration and transport of floating plastic debris. *Frontiers in Marine Science*, *8*. doi:10.3389/fmars.2021.621062

Small, J., Hallock, Z., Pavey, G., & Scott, J. (1999). Observations of large amplitude internal waves at the Malin Shelf edge during SESAME 1995. *Continental Shelf Research*, *19*(11), 1389-1436. doi:10.1016/S0278-4343(99)00023-0

Tensubam, C. M., Raju, N. J., Dash, M. K., & Barskar, H. (2021). Estimation of internal solitary wave propagation speed in the Andaman Sea using multi-satellite images. *Remote Sensing of Environment*, *252*. doi:10.1016/j.rse.2020.112123

Vlasenko, V., & Stashchuk, N. (2015). Internal tides near the Celtic Sea shelf

break: A new look at a well known problem. *Deep Sea Research Part I: Oceanographic Research Papers*, *103*, 24-36. doi:10.1016/j.dsr.2015.05.003

Woodson, C. B. (2018). The fate and impact of internal waves in nearshore ecosystems. *Annual Review of Marine Science*, *10*, 421-441. doi:10.1146/annurev-marine-121916-063619

Zeng, L., Wang, D., Chen, J., Wang, W., & Chen, R. (2016). SCSPOD14, a South China Sea physical oceanographic dataset derived from in situ measurements during 1919-2014. *Scientific Data*, *3*. doi:10.1038/sdata.2016.29

Zhang, S., Alford, M. H., & Mickett, J. B. (2015). Characteristics, generation and mass transport of nonlinear internal waves on the Washington continental shelf. *Journal of Geophysical Research: Oceans*, *120*(2), 741-758. doi:10.1002/2014JC010393

Zhang, X., & Li, X. (2020). Combination of satellite observations and machine learning method for internal wave forecast in the Sulu and Celebes seas. *IEEE Transactions on Geoscience and Remote Sensing*, *59*(4), 2822-2832. doi:10.1109/TGRS.2020.3008067

Zhao, Z., Klemas, V., Zheng, Q., & Yan, X. H. (2004). Remote sensing evidence for baroclinic tide origin of internal solitary waves in the northeastern South China Sea. *Geophysical Research Letters*, *31*(6). doi:10.1029/2003GL019077

Zhao, Z., Liu, B., & Li, X. (2014). Internal solitary waves in the China seas observed using satellite remote-sensing techniques: A review and perspectives. *International Journal of Remote Sensing*, *35*(11-12), 3926-3946. doi:10.1080/01431161.2014.916442